Analysis of the Combined Strengthening Effect of Solute Atoms and Precipitates on Creep of Aluminum Alloys

Ricardo Fernández[a],*, Gizo Bokuchav[b], Isaac Toda-Caraballo[a], Giovanni Bruno[c,d],Vitalii Turchenko[b], Yulia Gorshkova[b], and Gaspar González-Doncel[a]

[a] Department of Physical Metallurgy. Centro Nacional de Investigaciones Metalúrgicas (CENIM) C.S.I.C. Av. de Gregorio del Amo No. 8, Madrid E-28040, Spain

[b] Frank Laboratory of Neutron Physics. Joint Institute for Nuclear Research. Joliot-Curie Str. 6, Dubna 141980, Russia

[c] Bundesanstalt für Materialforschung und -prüfung (BAM). Unter den Eichen 87, Berlin D-12200, Germany

[d] Institute of Physics and Astronomy. University of Potsdam. Karl-Liebknecht-Str. 24-25, Potsdam 14476, Germany

Abstract: The creep strengthening mechanisms in (age-hardenable) aluminum alloys are analyzed on the basis of a new microstructural study of powder samples, an analysis of a comprehensive revision of creep data from the literature, and a new modeling approach. A strategy based on the strength difference (SD) method to separate the contributions of solid solution atoms and precipitates to creep strengthening is proposed. The new methodology considers the combination of the two contributions avoiding the need of a threshold stress term in the creep equation. The contribution of both precipitates and solid solution is taken into account by means of the analysis of the lattice parameter variation with aging time. For this study, powders of two commercial AA2xxx alloys have been analyzed using diffraction methods. The experimental results are modeled using Lubarda's approach combined with the SD method.

Keywords: aluminum, creep, diffraction, precipitation, solute atoms

1. Introduction

Aluminum alloys are good structural materials for component manufacturing requiring low weight and high strength. Their good properties must be extended to the high-temperature regime, >473 K (>200 ℃), if one wants to replace titanium and iron-based alloys, e.g., in engine parts and heat exchangers in the transportation sector [1]. The creep behavior of aluminum and its alloys processed by ingot metallurgy has been extensively investigated [2–15]. This behavior is commonly studied on the basis of the secondary or steady-state regime (where it is assumed that the changes in the microstructure occurring during that state are minimal). So, the so-called steady-state strain rate, $\dot{\varepsilon}$ss, depends on the temperature, T, and the applied stress, σ, according to the well-known semi-empirical power law creep equation [16,17]

$$\dot{\varepsilon}_{ss} = K \left(\frac{\sigma}{G}\right)^n \exp\left(-\frac{Q_c}{RT}\right) \qquad (1)$$

where K is a microstructure-dependent constant, n is the stress exponent, G is the shear modulus, Q c is the activation energy for creep, and R is the universal gas constant. One of the well-accepted findings is that the process of dislocation motion during creep of pure aluminum is controlled by diffusion inasmuch as Q c is usually identified with the activation energy for atom self-diffusion (Q_L 142 kJ mol^{-1}) [17,18]. This mechanism is also valid for some solid solution binary alloys such as Al–Mg [19–21]. However, the chemical composition of alloys generates a much more complex scenario. In the general case, e.g., in age-hardenable alloys, the presence of both solute atoms and particles/precipitates, commonly present in aluminum alloys, strongly affects Q c. In fact, different values are reported for different alloys.[22] As a consequence, little agreement is found in the literature on the mechanisms that govern creep of aluminum alloys, in particular age-hardenable alloys.[11,12,23–26] In these alloys, the problem is further complicated when the creep tests are carried out at temperatures at which precipitation evolves.[4,22] Precipitation plays a crucial role in the creep behavior because it influences dislocation dynamics [17,22]. In age-hardenable aluminum alloys, there are two main strengthening contributions from the alloying elements: the atoms that remain in solid solution and the precipitates. The associated strengthening mechanisms are strongly dependent on the heat treatment (HT) underwent by the alloy. Short treatment times and low temperatures produce small

precipitates, which reinforce the alloy against creep deformation significantly. On the contrary, long exposures at high temperatures produce large, incoherent, precipitates that are overcome by dislocations easily. So, their strengthening effect is significantly reduced [27]. However, even in overaged conditions, alloying elements in solid solution contribute to creep strengthening with respect to pure aluminum [11, 12]. The improved creep resistance associated with atoms in solid solution in binary alloys has been related to the low diffusivity of heavy atoms, such as Fe and Mn [28]. In summary, the contribution of alloying elements, both in solid solution and precipitates, must be studied for a rigorous analysis of the creep phenomenon. This contribution is considered in the literature [8, 29] as the simple arithmetic sum of the individual ones. As creep is a time-dependent deformation phenomenon, this strategy is unrealistic, and other approaches must be considered for a rigorous analysis of the contribution of different creep strengthening mechanisms.

Herein, the strength difference (SD) method, which compares the creep strength of a given alloy with that of the pure metal, is used to analyze the strengthening contributions in age-hardenable aluminum alloys. This method has demonstrated its capability to separate strengthening contributions from creep data in different materials.[11] Taking advantage of the fact that the precipitation sequence in most aluminum alloys is well known,[30–33] the effect of these creep strengthening contributions can be studied more rigorously considering that this precipitation evolution is taking place during creep. In the complex frame of age-hardenable alloys, it is necessary to combine the SD method with other tools that allow quantifying the contribution of each alloying element, either to solid solution or to precipitation strengthening. One of the most important approaches in the strategy that will be used in the present research is the use of powder samples. The precipitation kinetics in powder, however, are not exactly the same as in bulk samples undergoing creep at high temperature. As known, the applied stress responsible of creep may alter significantly the precipitation kinetics [33–37]. In fact, a compressive stress in a two-stage creep-aging process provides smaller grain boundary precipitates and narrower precipitate free zones.[38] On the contrary, it is also crucial to minimize the possible contribution of residual stresses (mainly macroscopic). These stresses can modify microstructural parameters (e.g., the lattice spacing) significantly and would prevent separating solute and precipitates contributions to creep strengthening.

Among the available microstructural analysis techniques that will be used in this research to overcome the aforementioned barriers are the diffraction methods. It is well proven the suit-

ability of diffraction (phase analysis) to study precipitation in metals [39, 40]. In fact, it is ideal for the lattice spacing determination and, therefore, very sensitive to solid solution content in aluminum alloys [41]. In this research, the amount of solid solution elements will be calculated by comparing the diffraction data and Lubarda's modeling predictions. Lubarda's approach has demonstrated [42] its suitability to account for the lattice parameter of complex solid solution alloys. In parallel, it will be shown that Rietveld refinement of diffraction data allows extracting the evolution of the precipitate size and microstrain (type III). The contribution of type III strains must be considered for a comprehensive analysis of diffraction data. Finally, quantitative analysis of scanning electron microscopy (SEM) images will complement the microstructural framework for large incoherent precipitates, not detected by diffraction (lattice para- meter variation).

The main objective of the work is to separate the strengthening contributions of solute atoms and precipitates on creep of aluminum alloys. The AA2014 and AA2124 alloys have been selected to study the microstructure evolution during aging because they are among the most well-known age-hardenable aluminum alloys for high-temperature applications. Furthermore, creep studies on these alloys are available in the open literature. While the two alloys are compositionally similar, they contain, particularly, quite different Si, Mg, and Mn concentrations. This will help to better separate the effect of the main alloying elements. In fact, it will be shown that the experimental data coupled with thermodynamic simulations allow drawing significant conclusions about the contributions of solid solution and precipitation to creep strengthening, not only in these two AA2xxx alloys but also in various other aluminum alloys. For this purpose, a thorough literature review data on the creep of pure aluminum and other Al alloys has been conducted here for the first time.

2. Experimental Section

2.1. Powder Characteristics. Chemical Composition and Heat Treatments

To quantify the evolution of solid solution and precipitates, powders of commercial AA2xxx series, specifically AA2014 and AA2124 sieved below 50 μm, have been studied. The chemical composition of the powders is shown in Table 1 (mass% SD) and (at%). This was determined by glow discharge optical emission spectroscopy (GD-OES).

Powder samples underwent HTs consisting of a solutionizing step, 813 K for 90 min, followed by water quenching at 300 K. For this purpose, the powders were wrapped in aluminum foil. Despite some surface oxidation of the particles, this procedure facilitated heat transfer which allowed increasing the quenching speed, thereby leading to a nearly precipitate-free solid solution. The initial microstructure of the studied alloys was defined by the T4 HTs that provided a full solid solution of alloying elements in the aluminum matrix. After the quenching step and a soaking time of 5 min at room temperature (RT), further HTs for 0.1, 1, 3, 10, and 100 h at 523 K were conducted.

2.2. Neutron Diffraction and Data Analysis

Neutron diffraction spectra were acquired from all the AA2014 and AA2124 powders heat treated as described earlier. Standard Ø8 mm vanadium containers were utilized, and counting times of about 12 h per spectrum were used. All neutron time-of-flight (TOF) diffraction experiments were performed on the Fourier stress diffractometer (FSD) at the IBR-2 pulsed reactor in FLNP JINR (Dubna, Russia) [43]. A special correlation technique at the long-pulse neutron source, i.e., a combination of the fast Fourier chopper for the primary neutron beam intensity modulation and the reverse time-of-flight (RToF) method for data acquisition, was used on FSD. This allowed obtaining a high resolution ($\Delta d/d \approx 2 \div 4 \cdot 10^{-3}$) over a wide range of interplanar spacing d_{hkl} for a relatively short flight distance between the chopper and the sample position ($L = 5.55$ m).

All main diffraction peaks from the Al phase were indexed in the frame of the face centered cubic structure (space group Fm3m) with lattice parameter $a \approx 4.050$ Å. The measured diffraction spectra were processed by MRIA program for full profile analysis, based on the Rietveld method [44,45]. A procedure to calculate microstrains (type III) from RToF data implemented in MRIA (similar to the Williamson–Hall peak broadening analysis [46]) had also been used.

2.3. X-Ray Diffraction and Data Analysis

As minority phases could not be reliably observed in the ND spectra, the crystallographic structure and phase composition of the samples were also examined by RT X-ray diffraction (XRD). An EMPYREAN diffractometer (PANalytical) with Co Kα incident radiation was used. The XRD spectra were measured with exposure time of 12 h for each sample. Using Rietveld analysis of XRD data by the FullProf program [47], the structural characteristics of all observed phases were

obtained, i.e., lattice parameter, phase volume fraction, microstrain, and crystallite size. Diffraction peak broadening for Al and the θ phases was mainly due to the presence of microstrains, while the crystallite size effect was negligible. On the contrary, it was observed that the peak profile broadening of the θ 0 phase due to crystallite size effect was dominant.

2.4. SEM and Image Analysis

SEM samples were prepared by grinding using sand papers, and polishing using diamond paste down to 1 μm. A final polishing step using colloidal silica at low pressure was used. SEM observations were performed utilizing a Hitachi 2100 J cold cathode microscope, operating at 10 mm working distance and 15 kV accelerating voltage. The brightness/contrast and gray threshold levels of the original SEM images were manually modified for each image to minimize the gray-level gradient around particles. The images were binarized and used for quantitative image analysis conducted using ImageJ analysis software [48]. At the magnification used (10k), the smallest of the major axes of precipitates was fixed at 25 nm. This was due to errors in size determination below this threshold value related to "noise" artifacts arising during image treatment.

3. Results

3.1. Analysis of Creep Literature Data

The literature data of the normalized steady-state strain rate, $\frac{\dot{\varepsilon}_{SS}kT}{GbD_L}$ (with k the Boltzmann's constant, b the Burgers vector in aluminum, and DL the self-diffusion coefficient of atoms in the aluminum lattice), versus normalized applied stress, σ/G, are shown in Figure Ap.1, Supporting Information (literature sources are cited in the figure in brackets). They encompass various aluminum alloys and pure aluminum [49–51]. All alloys show an increase in creep strength with respect to pure aluminum. It was noted that the alloys tested at temperatures below about 550 K present a very high strength increment or creep strength increase with respect to pure aluminum. Under such conditions, the precipitation kinetics must be slowed down for the majority of aluminum alloys [52]. For this reason, it is reasonable to expect an important strengthening contribution related with small precipitates. It is also well accepted that the solid solution of some elements, mainly Mg, Fe, Mn, Cr, and Ti, in binary alloys, even at very low content, increases the creep resistance with respect to pure aluminum [28]. On the contrary, aluminum alloys overage very rapidly above 550 K (and

precipitates become large and fully incoherent). As the contribution of the Orowan mechanism (dislocations bowing these large particles) to creep strength must be very low at such temperatures, around 10 MPa, the strengthening effect observed in Figure Ap.1, Supporting Information, at temperatures above 550 K must be associated mainly with solute atoms, despite that the solubility of most of the alloying elements in aluminum, except Cu, Mg, and Zn, is very low [53]. Table 2 shows the chemical composition and the maximum solubility of alloy elements in the aluminum alloys studied in this work [29,53–58]. An overview of the possible precipitates formed in these alloys is shown in Table 3.

Intermetallic particles are also present in aluminum alloys. These particles also act as preferential sites for precipitation and pore formation in age-hardenable aluminum alloys [59]. Their size ranges from some micrometers to above 1 mm, depending on alloying element content and cooling rate. Therefore, they must not introduce a major strengthening effect in aluminum [28]. Consequently, the effect of these intermetallics will not be considered in the present work.

To analyze further the creep stress increase of the aluminum alloys, the SD method proposed by Fernández et al [60]. has been used. As mentioned earlier, this method allows calculating the normalized stress increment, $\Delta(\sigma/G)$, necessary for the alloys to creep at the same strain rate as pure aluminum. If this method is applied to the data of Figure Ap.1, Supporting Information, the plots of Figure 1 are obtained. In this figure, the normalized stress increment data are shown as a function of normalized stress at different temperatures. Although a complex scenario would be expected in Figure 1 given the complex microstructure of the commercial alloys, it shows, however, that two clear different regimes are visible, depending on the creep temperature: above 550 K, the alloys present a small stress increment, and the $\Delta(\sigma/G)$ versus (σ/G) dependence shows a linear behavior (note, furthermore, that the extrapolated lines cross the origin). It is proposed that this (linear) stress increment is due to the presence of solute atoms, regardless of the alloy composition. Below 550 K, however, the stress increment is significantly larger, and presents a nonlinear behavior with (σ/G). This behavior will be associated with the solid solution effect and with the presence of small precipitates. The alloy AA5083 does not fall in either category. This result can be associated with the fact that it is not an age-hardenable alloy.

To asses these hypotheses, the literature data shown in Figure Ap.1, Supporting Information, have been separated into two groups (Figure 2a,b): creep data at high temperature (>550 K) and at low temperature (<550 K), respectively. The strengthening effect of solid solution and precipitates in

each case will be analyzed in the examples of AA2014 and AA2124 alloys.

3.2. Evolution of the Matrix Lattice Parameter and Precipitate Volume Fraction

Figure Ap.2, Supporting Information, shows XRD spectra from powder samples of the AA2014 and AA2124 alloys treated from initial solid solution (T4) to overaged condition (100 h/523 K). In addition to diffraction peaks from the main phase of aluminum, peaks from θ and $\theta´$ precipitate phases were detected. Some peaks from pure silicon were also observed in the diffraction patterns of the AA2014 alloy. However, Si contribution is not relevant in the present case because it does not influence the creep behavior of these alloys. The Rietveld (global) refinement [61], the contribution of all individual phases, and the residues (differences between measured and calculated patterns) are also shown in Figure Ap.2, Supporting Information. The Al matrix lattice parameter evolution due to ageing, as deter- mined by Rietveld analysis of both ND and XRD data, is shown in Figure 3. The lattice parameters of the two alloys in T4 conditions are significantly smaller than that of pure aluminum (dashed line). This is due to the presence of copper atoms in solid solution, which reduces the lattice cell size [44, 62]. The presence of magnesium atoms, which is expected to increase the lattice parameter [62], is not sufficient to compensate the opposite effect of the Cu atoms. Subsequently, the ageing treatment at 523 K increases the matrix lattice parameter, due to copper depletion in solid solution. Cu precipitation leads to the formation of coherent CuAl2 precipitates [62]. This increase is small during the first stages of HT, up to 0.3 h, corresponding to the formation of Guinier–Preston (GP) zones and small precipitates. Between 0.3 and 10 h, the lattice parameter increases much more steeply.

This is due to the increase in precipitate volume fraction and size consistently with the results shown in Figure 4 and 5. Figure 4 shows the volume fraction variation of the different precipitates of the two alloys, determined by the Rietveld analysis [61]. Figure 5 shows the evolution with ageing time of the size of the small, $\theta´$, precipitates, also determined from Rietveld analysis. Finally, at aging times over 10 h, the Ostwald ripening mechanism controls the precipitation process, and large precipitates (>250 nm) are found, as also confirmed by quantitative SEM picture analysis (Figure 6). The diffusivity of copper solute atoms can be influenced by the presence of Si in the AA2014 alloy. This influence is manifested in volume fraction differences mainly between 1 and 3 h for AA2014 and AA2124 alloys (Figure 4). The migration of Si in solid solution to metallic particles modifies the ratio of the volume fractions of $\theta´$ and θ. However, this effect is secondary in comparison

8

to that of the Cu content regarding the creep behavior. In fact, in overaged condition, 100 h at 523 K, the precipitate content is higher in the AA2014 alloy, corresponding to a higher Cu content, despite the presence of Si.

From Figure 4 it can also be seen that the fraction of incoherent $\theta 0$ precipitates increases following the same sigmoidal curve displayed by the evolution of the lattice parameter, i.e., solid solution (Figure 3). This is something expected because precipitates grow at the expense of solute atoms according to literature data on the precipitation process. In both alloys, AA2014 and AA2124, the volume fraction of θ' precipitates is around 8%, in the over-aged condition (100 h) (Figure 4). Moreover, the evolution of θ precipitates volume fraction is very similar for the two alloys. A maximum of 4% of θ precipitates is found after 100 h treatment time (overaged state). This information in conjunction with the evolution of the θ precipitate size with aging time, shown in Figure 5, provides information about the difference between the two alloys as far as precipitate nucleation is concerned. According to this result it is deduced that the AA2014 presents a more homogeneous distribution of small precipitates than the AA2124 alloy.

In summary, the lattice parameter evolution with annealing time should be attributed mainly to the variation of alloying elements in solid solution [63], i.e., Cu, Si, Mn, and Mg in AA2014 and AA2124 alloys. It will be seen that modeling the solid solution effect on the lattice parameter allows quantifying the effect of solid solution and that of precipitates on diffraction data.

3.3. Microstructure

Combining diffraction and SEM techniques allowed covering the broad range of precipitate sizes found in aluminum alloys depending on HT conditions. This analysis is crucial to deepen into the particles effect on creep strengthening. SEM pictures of the AA2014 powder samples in different HT conditions are shown in Figure 6, together with the size distribution of precipitates. The analysis for AA2124 yielded to similar results, which are not reported here for the sake of brevity. The alloy presents needle-shaped precipitates. Their major axis mean size increases from around 100 nm at 0.3 h of HT to 300 nm in the overaged condition (100 h). Also, the spatial arrangement of the precipitates depends on HT time: for short times (0.3 h), they are located at grain boundaries (Figure 6). After 1 h HT, also grain interiors are decorated with precipitates. Their spatial distribution becomes very homogeneous after 10 h of HT. Finally, it is worth mentioning that a stereological correction

was applied to the SEM pictures to allow quantitative analysis and comparison with the XRD data analysis.

3.4. Modeling of the Matrix Lattice Parameter Evolution

The precipitation sequences for the AA2014 and AA2124 have been classically described [26,33,63] as:

$\alpha_{ss} \rightarrow \alpha + GPZ \rightarrow \alpha + \lambda' \rightarrow \alpha + \lambda' + \theta' \rightarrow \alpha + \lambda$ $(Al_5Cu_2Mg_8Si_5) + \theta(CuAl_2)$ for the AA2014 alloy and

$\alpha_{ss} \rightarrow \alpha + GPZ \rightarrow \alpha + S' \rightarrow \alpha + S' + \theta' \rightarrow \alpha + S$ $(CuMgAl_2) + \theta(CuAl_2)$ for the AA2124 alloy.

Considering the low Mg content in the AA2014 powder alloy of the present work, the amount of λ (A15Cu2Mg8Si5) precipitates must be very low. A small quantity of λ phase could possibly correspond to the unindexed peaks shown in Figure Ap.2, Supporting Information, for this alloy. On the contrary, the expected presence of secondary precipitates S (CuMgAl2) in the AA2124 alloy has not been detected at all here, Figure Ap.2, Supporting Information. It was deduced that both the S- and the λ phase contents were negligible in the present samples probably because they are in powder form instead of bulk.

The variation in lattice parameter of both alloys was modeled considering the effect of both solute atoms and θ precipitates. For this purpose, Lubarda's approach [42] was first used to predict the lattice parameter of the aluminum alloys considering the effect of solute atoms. To this aim, experimental data on different alloys from the literature were used. This allowed calculating the matrix lattice parameter in T4 conditions, assuming that all species were fully solutionized. Second, the effect of the θ precipitates was included in the model to calculate the evolution of the matrix lattice parameter as a function of HT time.

In this approach, the lattice parameter of a binary alloy is calculated using the lattice parameter of pure Al, and the apparent size of the solute atom in the crystal structure of the solvent [42]. The use of this approach has also been successfully extended in multicomponent alloys [64,65]. In Lubarda's approach, the lattice parameter, a, of a cubic system is approximated by

$$a = (a_0{}^3 + \sum_{i=1}^{N} 4\pi R_i x_i m \gamma_i C_i)^{1/3} \qquad (2)$$

where a_0 is the solvent lattice parameter, R_i is its Wigner–Seitz atomic radius of species i (i 1,N), m is the number of atoms per unit cell and $a_0{}^3$ is its corresponding volume, x_i is the volume

10

fraction of solute atom species i, and γ_i and C_i are functions of the elastic constants and of the atomic radius of the solvent and solute i [42]. This model was, first, fitted to the available literature data, and the parameters θ, R_i, γ_i, and C_i were calibrated for the species contained in the alloys under study. In other words, the aforementioned parameters were fitted until the calculated and measured lattice parameters did not match (Figure 7). Experimental data of binary, ternary, and quaternary systems of Al solid solutions were extracted from ref. [66]. They include the effect of solutes such as Cu6, Mg15, Si1.5, Mn3.5, Cu0.9– Mg1.8, Mg17–Si1, Si2–Fe0.16, Mg17–Fe0.5, and Mg17–Fe0.5–Si1 (where the number represents the maximum concentration in at%). Successively, the model was used to predict the lattice parameters of the specific AA2014 and AA2124 alloys using the measured values of x_i (for each species, see Table 1). Due to the low solute concentration, it was assumed that interactions only occur between each individual solute species and the solvent, i.e., solute–solute interactions are considered negligible.

The Al matrix lattice parameter of both AA2014 and AA2124 powder alloys in the T4 conditions obtained experimentally from X-ray and ND measurements are compared with the model results in Figure 8a (first point on the left). A good agreement between predicted and measured data is observed. At a third step, the variation of the alloy composition and the Al matrix lattice parameter due to the precipitation of the θ-phase with annealing time was analyzed. The precipitation was modeled by a typical nucleation, growth, and saturation sequence, using the Johnson– Mehl–Avrami– Kolmogorov (JMAK) equation [67] of the trans- formed fraction, f, at time t

$$f = f_{max}\left(1 - e^{-K't^p}\right) \tag{3}$$

where f max   is the maximum volume fraction transformed in the saturation sequence, K´ is a function of the reaction rate and the activation energy, and p is a parameter dependent on geometrical aspects of precipitates. The parameters K´ and p were fitted to the experimental data on the alloys under study (Figure 3) to obtain an analytical dependence of the volume fraction of θ precipitates with annealing time assuming that only Cu precipitates as $CuAl_2$ (based on the diffraction data shown earlier). For the sake of simplicity, a direct θ precipitation, instead of the typical sequence GPZ θ'', θ', θ, [64] was considered.

An atomic volume of 14.84 Å^3 was considered for θ precipitates [59]. It was also assumed that f max is associated to the maximum fraction of θ phase, corresponding to the Cu content of each alloy (4.2 wt% in AA2014 and 4.05 wt% in AA2124). The fitting parameters ($K' = 5 \times 10^{-5}$ s^{-1}

and $p = 1$) were obtained by minimizing the square difference between the measured Al matrix lattice parameter and the one calculated by means of Equation (2). This allowed us to simultaneously obtain the analytical dependence of the precipitate volume fraction, the lattice parameter (Figure 8a), and the amount of Cu in solid solution (Figure 8b) as a function of treatment time.

3.5. Internal Strains

The model predicts the lattice parameter evolution of both AA2014 and AA2124 powder alloy compositions with high accuracy (error below 0.01 Å), by considering only solid solution and θ precipitates. However, a discrepancy between calculations and experimental data appear at 1 h HT for AA2124 alloy (Figure 8a). This can be explained as follows. Another parameter that can be obtained from the Rietveld analysis is the microstrain (types II and III) introduced into the matrix during the HT. As only a microscopic residual stress can be present in powder samples, the stress analysis can be made considering that a macroscopic residual stress is absent. The evolution of the resulting microstrains is shown in Figure 9. Such microstrains must be caused by the intergranular strains (or the different strain carried by the neighboring grains) and by the lattice distortion resulting from the coherency between the precipitates and the matrix lattice. They are reflected in the diffraction peak broadening (compared with a standard and/or a reference sample).

The dependence of the microstrain as a function of annealing time shows a peak at 1 h HT time. As the model does not include microstrain effects, it can be concluded that the discrepancy between measured and calculated lattice parameter must be attributed to internal microstrain in the powder materials.

4. Discussion

The normalization procedure works correctly for pure Al and Al alloys, i.e., data at different temperatures for each alloy fall in the same line (Figure 2). This indicates the relevance of atom self-diffusion as the rate controlling mechanism for dislocation motion.[20] The shift between the pure Al curve and age- hardenable Al alloys, shown in Figure 2, suggests that the specific effect of solutes such as Mg, Cu, Zn, Si, Fe, Mn or Ti, and precipitates (and/or intermetallic particles) is not

considered by the standard normalization procedure.

In the case of binary solid solution alloys, the minimum creep strain rate can be described by the equation [20, 21]

$$\dot{\varepsilon}_{SS} = \frac{\pi \Omega kT}{(\alpha GM)^2}\sigma^3(A\sigma^2 + B\sigma + C)\left[\frac{D_{sol}D_L}{2\pi c_0 ln(r_2/r_1)D_L + (bkT)^2 ln\left(c^*/c_0^*\right)D_{sol}}\right] \qquad (4)$$

where Ω is the atomic volume; M is the Taylor factor; A, B, and C are the constants related to the ratio of mobile-to-total dislocation densities, taken from ref. [21]; D_{sol} is the solute diffusion coefficient; c_0 is the solute concentration in the aluminum matrix; r_2 and r_1 are the outer and inner cutoff radii of the solute, respectively; c^* and c_0^* are the vacancy concentration around dislocations and in equilibrium, respectively; and α is a geometrical parameter that describes the dislocation arrangement in the matrix alloy. Typical values of these parameters are shown in Table 4 for the solute atoms that introduce strong creep strengthening in aluminum alloys: Mg, Fe, and Mn.

The fractal nature of the dislocation structure generated during creep should be also included in this α parameter [23]. However, the effect of this fractal structure will not be considered here for the sake of simplicity. A further analysis of this microstructural factor is being the subject of future work.

In the case of Al–Mg alloys, the shift of σ/G data towards higher normalized stresses with respect to data on pure aluminum, Figure Ap.1, Supporting Information, was explained by the drag force mechanism during dislocation climb [21]. It is proposed that this normalized stress shift (creep strength increment) above 550 K, Figure 2a) is related to the presence of solid solution atoms, not only "light" atoms, such as Cu, Si, and Mg, but also heavy ones, such as Mn, Ti, and Fe. In fact, the chemical composition of most Al alloys includes more than five elements. Knipling et al. [68] and Nie et al. [69] state that only the elements that form precipitates must be considered to explain the observed creep strength increment. However, other authors claim that the contribution of heavy elements such as Fe, Mn, and Ti, not forming precipitates is also very important [27]. It is suggested that their low diffusivity in the Al lattice, which implies an increase of the activation energy for creep, must be compensated by an increase of stress, if $\dot{\varepsilon}_{SS}$ remains constant, Equation (4). Therefore, it is predicated that the creep behavior of aluminum alloys at temperatures >550 K can be described by Equation (4) in which the content of heavy atoms in solid solution (Table 2) is also taken into account.

It is assumed that at these temperatures the contribution of precipitates is negligible as they are fully over- aged. At temperatures above 550 K the strengthening contribution of large precipitates in Al alloys is around 10 MPa and for solute atoms it is larger than 40 MPa. The atom concentration in solid solution ranges from 0.056% in the case of Fe to typically 0.6% in the case of Mn in commercial aluminum alloys (Table 2). The behavior predicted by Equation (4) for these two cases is shown in Figure 2, green lines. The behavior of commercial alloys will be located between these two extreme compositions. A constant value of the geometrical parameter $\alpha = 0.3$ in Equation (4) was selected, following [21] (the enhanced diffusion effect introduced by the fractal dislocations structure is, as mentioned earlier, not considered to calculate $\dot{\varepsilon}_{SS}$). Despite this simplification, Equation (4) provides a very reasonable prediction of the experimental data (Figure 2a).

At tow temperatures, <550 K, the contribution of precipitation to creep strengthening in age-hardenable alloys is manifested in further additional curve shift to higher stresses, as well as to lower normalized $\dot{\varepsilon}_{SS}$, as, for example, in the case of AA2xxx series alloys (Figure 2b). There are two contributions to this strengthening. The solubility and diffusivity of solid solution atoms significantly diminish, as in the case of Fe and Mn. In this range of temperatures, it can be considered that only 0.056% of Fe is in solid solution being the solubility of Mn very low. The prediction of Equation (4) at 443 K considering this contribution is shown in Figure 2b. Figure 2 shows that the contribution of solid solution heavy atoms in creep strengthening is still relevant at low temperatures. In age-hardenable alloys, the contribution of precipitation to the strength increment (with respect to pure aluminum) depends on the precipitate size and on the inter-particle distance [25]. Bowing of dislocations around precipitates is the dominant reinforcing mechanism in this case. This mechanism was first described by Orowan [25]. The flow stress due to this mechanism, σ_{Or}, in the case of nonspherical precipitates (such as the laths shown in Figure 6) is given by Equation (5) [70–72], as follows

$$\sigma_{Or} = M \cdot \frac{Gb}{2\pi\sqrt{1-\nu}} \cdot \frac{ln\left(\frac{R_{eq}}{r_i}\right)}{\lambda} \qquad (5)$$

where ν is the Poisson ratio, R_{eq} is the outer cutoff radius, r_i is the inner cutoff radius of precipitates, and λ is the effective interparticle distance.

According to Equation (5), and considering the experimental data from Figure 4 and 5, it is found that the creep strength increment introduced by the Orowan mechanism lies between 115 and 135

MPa (at T = 443 K). In the calculation, the values $R_{eq} \sim [20-30]$ nm $r_i \sim [2-3]$ nm and the volume fraction of θ' precipitates of about 3–4% at peak age conditions for both alloys have been used.

At RT, the yield strength increment in alloys with respect to pure metals is explained by adding the Orowan stress to the Critical Resolved Shear Stress (CRSS) of the pure metal [73]. This additive contribution, successfully applied at RT, has also been used to explain the creep strengthening of aluminum alloys with respect to pure Al.[29] This term is classically introduced in the creep equation as a threshold stress [29,74]. However, the time dependent nature of strain in the creep regime is incompatible with this proposal. A realistic approach must combine creep strengthening and time-dependent strain evolution. In the case of aluminum alloys, the introduction of precipitate strengthening in the creep equation can be justified by the fact that a fraction of the dislocation population is trapped by the precipitates. Therefore, such dislocations do not contribute to creep deformation and the mobile/total dislocation density ratio is diminished. However, mobile dislocations undergo the total applied stress. The more general case that considers both the solute atoms and precipitates contributions to creep strengthening and the time-dependent strain evolution are combined in Equation (6).

$$\dot{\varepsilon}_{SS} = \frac{\pi \Omega k T}{(\alpha G M)^2} \sigma^3 \left(A(\sigma - \sigma_{0r})^2 + B(\sigma - \sigma_{0r}) + C \right) \left[\frac{D_{sol} D_L}{2\pi c_0 ln(^{r_2}/_{r_1}) D_L + (bkT)^2 ln(^{c^*}/_{c_0^*}) D_{sol}} \right] \quad (6)$$

where σ_{Or} is, as mentioned earlier, the Orowan contribution of nonspherical precipitates described by Equation (5). Equation (6) considers the normalized applied stress in the "natural" stress term, i.e., $(\sigma/G)^3$, and the effective stress $(\sigma - \sigma_{Or})$ in the mobile- to-total dislocation density ratio.

The Orowan stress, σ_{Or}, can be related to the dislocations anchored by the precipitates through the Taylor equation. The predictions of Equation (6), using this approach, are shown in Figure 2b for the AA2xxx alloys (references are cited in the figure). These predictions properly reproduce the creep behavior of aluminum alloys containing precipitates.

The AA7010 alloy shows a smaller resistance to creep than the AA2xxx series, probably due to the presence of larger precipitates in the AA7010 alloy. This calls for further microstructural characterization of AA7xxx alloys, which is, however, out of the scope of the present work. Bowing of dislocations around precipitates is, therefore, also a reinforcing mechanism at low creep temperatures (in the present work, at temperatures <550 K) in aluminum alloys. However, this

contribution is smaller than that of heavy atoms in solid solution (Figure 2b).

The displacement of the normalized $\dot{\varepsilon}$ versus σ curves to lower normalized $\dot{\varepsilon}$ can also be related to the fact that the precipitation process, even in overaged conditions, is a vacancy diffusion-assisted mechanism. In fact, the term related to vacancies concentration $\ln(c^*-c_0^*)$ in Equation (4) and (6) must increase if $\dot{\varepsilon}$ decreases. It is suggested that this corresponds to a decrease in vacancies available to assist the creep process. Those vacancies are rather used to assist the precipitation evolution (the coarsening process). As the vacancy equilibrium concentration depends only on the temperature, these vacancies must be shared by the two processes (creep and coarsening).

Finally, it is noted that Equation (6) involves, both, a creep strength shift and a strain rate shift combined in a nonlinear fashion. It therefore comprehensively encompasses the two interrelated phenomena of precipitation and solid solution in aluminum alloys, thereby casting new light on the complex mechanisms of creep strengthening. The classic creep equation, linking normalized $\dot{\varepsilon}$ to normalized σ in Al–Mg alloys [52], can be generalized to other aluminum alloys.

5. Conclusions

A description of the creep behavior of aluminum alloys is pro- posed, based on the combined contributions of solid solution atoms and precipitates. Physically, these contributions are justified by the facts that creep is a diffusion-controlled dislocation motion process, and that the thermally stable nanometric particles hinder dislocation motion, thereby introducing a strengthening effect. The proposed model explains the creep behavior of aluminum through the variation of the volume fraction of solute atoms, the diffusion coefficient D, the effective stress, σ_{eff}, and the vacancy concentration. The model is validated by experimental creep data of AA2014 and AA2124 aluminum alloys reported in the literature. The main conclusions of this work are 1) diffraction techniques (and the Rietveld analysis of diffraction data) combined with simulations (Lubarda's approach) allow determining solid solution and precipitates content as a function of creep (HT) time; 2) the SD method allows determining the solid solution (effective diffusion) and precipitate (Orowan) contributions to creep strengthening of aluminum alloys; and 3) the creep strength increment stress shift with respect to pure Al in aluminum alloys at high temperatures (>550 K) is associated with the low diffusivity of heavy atoms in the Al lattice. At low temperatures (<550 K) this stress increment is

also associated with the dislocation entanglement caused by the presence of precipitates, and to the sequestration of vacancies at the precipitate boundaries. In this case, a nonlinear equation is proposed, which encompasses the contribution of mobile dislocations and precipitates, thereby explaining the contemporary strain and stress shift of the classic creep curves.

References

[1] J. A. Lee, P.-S. Chen, US Patent 6,918,970, 2005.

[2] L. Chen, G. Zhao, J. Gong, X. Chen, M. Chen, J. Mater. Eng. Perf. 2015, 24, 5002.

[3] Y. C. Lin, Q.-F. Li, Y.-C. Xia, L.-T. Li, Mater. Sci. Eng. A 2012, 534, 654.

[4] E. Gariboldi, F. Casaro, Mater. Sci. Eng. A 2007, 462, 384.

[5] Y. C. Lin, L. T. Li, Y. C. Xia, Comput. Mater. Sci. 2011, 50, 2038.

[6] S. Spigarelli, M. Cabibbo, E. Evangelista, J. Bidulska, J. Mater. Sci. 2003, 38, 81.

[7] F. Bardi, M. Cabibbo, E. Evangelista, S. Spigarelli, M. Vukcevic, Mater. Sci. Eng. A 2003, 339, 43.

[8] G. R. Ebrahimi, A. Zarei-Hanzaki, M. Haghshenas, H. Arabshahi, J. Mater. Proc. Technol. 2008, 206, 25.

[9] K. E. Tello, A. P. Gerlich, P. F. Mendez, Sci. Technol. Weld. Joining 2010, 15, 260.

[10] H. Sato, K. Maruyama, H. Oikawa, Mater. Sci. Eng. A 1997, 234236, 1067.

[11]   R. Fernández, G. González-Doncel, J. Alloys Compd. 2007, 440, 158.

[12]   R. Fernández, G. González-Doncel, Acta Mater. 2008, 56, 2549.

[13]   H. Burt, B. Wilshire, Metall. Mater. Trans. A 2006, 37, 1005.

[14]   Y.-Q. Jiang, Y. C. Lin, C. Phaniraj, Y.-C. Xia, H. M. Zhou, High Temp. Mater. Processes 2013, 32, 533.

[15]   Y. Li, T. G. Langdon, Acta Mater. 1999, 47, 3395.

[16]   O. D. Sherby, J. L. Lytton, J. E. Dorn, Acta Meter. 1957, 5, 219.

[17]   O. D. Sherby, P. M. Burke, Prog. Mater. Sci. 1968, 13, 323.

[18]   O. D. Sherby, J. Weertman, Acta Meter. 1979, 27, 387.

[19]   H. Oikawa, K. Honda, S. Ito, Mater. Sci. Eng. A 1984, 64, 237.

[20]   R. Fernández, G. González-Doncel, Mater. Sci. Eng. A 2012, 550, 320.

[21]   S. Takeuchi, A. S. Argon, Acta Metall. 1976, 24, 883.

[22]   H.-R. Erfanian-Naziftoosi, E. Rincon, H. F. Lopez, Metall. Mater. Trans. A 2016, 47, 4258.

[23]   R. Fernández, G. Bruno, G. González-Doncel, J. Appl. Phys. 2018, 123, 145108.

[24]   J. S. Robinson, R. L. Cudd, J. T. Evans, Mater. Sci. Technol. 2003, 19, 143.

[25]   C. B. Fuller, D. N. Seidman, D. C. Dunand, Scr. Mater. 1999, 40, 691.

[26]   Y. C. Lin, Y. C. Xai, Y. Q. Jiang, L.-T. Li, Mater. Sci. Eng. A 2012, 556, 796.

[27]   E. Orowan, in Symp. on Internal Stresses in Metals and Alloys, Institute of Metals, London 1948, p. 451.

[28]   O. D. Sherby, O. A. Ruano, Mater. Sci. Eng. A 2005, 410–411, 8.

[29]   J. Zhang, Y. Deng, X. Zhang, Mater. Sci. Eng. A 2013, 563, 8.

[30]   R. K. W. Marceau, C. Qiu, S. P. Ringer, C. R. Hutchinson, Mater. Sci. Eng. A 2012, 546, 153.

[31]   M. J. Styles, R. K. W. Marceau, T. J. Bastow, H. E. A. Brand, M. A. Gibson, C. R. Hutchinson, Acta Mater. 2015, 98, 64.

[32]   I. Dutta, S. M. Allen, J. Mater. Sci. Lett. 1991, 10, 323.

[33]   M. J. Starink, Int. Mater. Rev. 2004, 49, 191.

[34]   G. Sauthoff, J. Phys. IV 1996, 06, C1.

[35]   G. Xiaobin, D. Yunlai, Z. Xinming, Mater. Sci. Eng. A 2018, 730, 187.

[36]   Y. C. Lin, Y.-C. Xia, Y.-Q. Jiang, H.-M. Zhou, L.-T. Li, Mater. Sci. Eng. A

2013, 565, 420.

[37]   Y. C. Lin, Y.-C. Xia, Y.-Q. Jiang, H.-M. Zhou, L.-T. Li, Mater. Sci. Eng. A
2012, 556, 796.

[38]   Y. C. Lin, X.-B. Peng, Y.-Q. Jiang, C.-J. Shuai, J. Alloys Compd. 2018,
743, 448.

[39]   G. D. Preston, Proc. R. Soc. London Ser. A 1938, 167, 526.

[40]   O. Novelo-Peralta, G. González, G. A. Lara-Rodríguez, Mater. Charact.
2008, 59, 773.

[41]   M. W. Johnson, L. Edwards, P. J. Withers, Phys. B 1997, 234–236, 1141.

[42]   V. A. Lubarda, Mech. Mater. 2003, 35, 53.

[43]   G. Bokuchava, Crystals 2018, 8, 318.

[44]   T. J. Bastow, S. Celotto, Acta Mater. 2003, 51, 4621.

[45]   V. B. Zlokazov, V. V. Chernyshev, J. Appl. Crystallogr. 1992, 25, 447.

[46]   P. W. Stephens, J. Appl. Cryst. 1999, 32, 281.

[47]   J. Rodríguez-Carvajal, Phys. B 1993, 192, 55.

[48]   J. Schindelin, I. Arganda-Carreras, E. Frise, V. Kaynig, M. Longair, T. Pietzsch, S. Preibisch,
C. Rueden, S. Saalfeld, B. Schmid, J. Y. Tinevez, D. J. White, V. Hartenstein, K. Eliceiri, P.
Tomancak, A. Cardona, Nat. Meth. 2012, 9, 676.

[49]   I. S. Servi, N. J. Grant, Trans. AIME 1951, 191, 917.

[50]   I. S. Servi, N. J. Grant, Trans. AIME 1951, 191, 909.

[51]   S. Straub, W. Blum, Scr. Metall. 1990, 24, 1837.

[52]   E. A. Marquis, D. N. Seidman, D. C. Dunand, Acta Mater. 2003, 51, 4751.

[53]   S. Hori, H. Tai, E. Matumoto, J-Stage 1984, 34, 377.

[54]   ASM Handbook Volume 3: Alloy Phase Diagrams (Eds: H. Okamoto,
M. E. Schlesinger, E. M. Mueller), ASM International, Materials Park, OH 2016.

[55]   S.-I. Fujikawa, Y. Oyobiki, K.-I. Hirano, J-Stage 1979, 29, 331.

[56]   M. Nishio, S. Nasu, Y. Murakami, J-Stage 1970, 34, 1173.

[57]   Phase Equilibria, Crystallographic and Thermodynamic Data of Binary Alloys (Ed: B.
Predel), Landolt-Börnstein New Series IV/12A Supplement to IV/5A. Al – Mn (Aluminum –
Manganese) 2006.

[58]   L. F. Mondolfo, Aluminum alloys: Structure and Properties, Butterworth-Heinemann,

Oxford/Stoneham, MA 1976, pp. 842–882.

[59]   J. A. Taylor, Proc. Mater. Sci. 2012, 1, 19. 11th International Congress on Metallurgy & Materials SAM/CONAMET 2011.

[60]   R. Fernández, E. García-Alonso, G. González-Doncel, Rev. Met. 2005, 41, 239.

[61]   H. M. Rietveld, J. Appl. Crystallogr. 1969, 2, 65.

[62]   R. A. Young, The Rietveld Method, Oxford University Press, Oxford/ New York 1995.

[63]   A. Steuwer, M. Dumont, M. Peel, M. Preuss, P. J. Withers, Acta Mater. 2007, 55, 4111.

[64]   I. Toda-Caraballo, P. E. J. Rivera-Díaz-del-Castillo, Acta Mater. 2015, 85, 14.

[65]   I. Toda-Caraballo, Scr. Mater. 2017, 127, 113.

[66]   W. B. Pearson, Handbook of Lattice Spacings and Structures of Metals and Alloys, Pergamon Press, London 1958.

[67]   S. Jun, H. Zhang, A. Bechhoefer, Phys. Rev. E 2005, 71, 011908.

[68]   K. E. Knipling, D. C. Dunand, D. N. Seidman, Z. Metallkd. 2006, 97, 246.

[69]   F. Nie, B. C. Muddle, Acta Mater. 2008, 56, 3490.

[70]   M. R. Ahmadi, B. Sonderegger, E. Povoden-Karadeniz, A. Falahati, E. Kozeschnik, Mater. Sci. Eng. A 2014, 590, 262.

[71]   C. Carry, J. L. Strudel, Acta Metal. 1977, 25, 767.

[72]   C. Carry, J. L. Strudel, Acta Metal. 1978, 26, 859.

[73]   J. F. Nie, B. C. Muddle, J. Phase Equilib. 1998, 19, 543.

[74]   M. E. Krug, D. N. Seidman, D. C. Dunand, Mater. Sci. Eng. A 2012, 550, 300.

Table 1. Chemical composition of the studied AA2xxx aluminum alloys powders.

Alloy	Cu	Si	Fe	Mn	Mg	Cr	Zn	Zr	Ti
2014 (wt%)	4.40 0.10	0.720 0.01	0.083 0.002	0.012	0.52 0.01	<0.00 2	<0.00 5	—	<0.05
2124 (wt%)	4.17 0.05	0.113 0.005	0.104 0.002	0.59 0.01	1.50 0.01	<0.00 2	<0.01 1	—	<0.05
Atomic mass	63.55	28.09	55.85	54.94	24.32	52.00	65.38	—	47.87
Max. solubility (wt%/at%)	5.67/2.48	1.65/1.59	0.052/0.025	1.82/0.90	14.9/16.26	0.77/0.4	88.2/66.4	—	1/0.57
2014 (at%)	1.92	0.71	0.04	0.01	0.59	0.001	0.002	—	0.029
2124 (at%)	1.82	0.11	0.05	0.30	1.71	0.001	0.005	—	0.029

Table 2. Chemical composition of the commercial aluminum alloys from literature summarized in Figure 1. Values in bold are included from the handbook and from ref [42] because this information is not available in the papers.

Alloy [wt%]	Cu	Si	Fe	Mn	Mg	Cr	Zn	Zr	Ti	Heavy [S.S.]
2014	4.40	0.90	0.70	0.80	0.50	0.1	0.25	—	0.15	1.00
2024	4.40	0.42	0.50	0.50	1.32	0.1	0.28	—	0.15	0.75
2124	4.17	0.11	0.10	0.59	1.50	<0.002	<0.01	—	<0.05	0.70
5083	0.10	0.40–0.70	0.40	0.40–0.10	4.0–4.9	0.05–0.25	0.25	—	0.15	0.60
6061	0.27	0.45	0.15	0.002	0.96	0.16	—	—	—	—
7010	1.5–2.0	0.12	0.15	0.10	2.1–2.6	0.05	5.7–6.7	0.10–0.16	0.06	0.40
7050	2.0–2.6	0.12	0.15	0.10	1.9–2.6	0.04	5.7–6.7	0.08–0.15	0.06	0.40
7075	1.2–2.0	0.40	0.50	0.10	2.1–2.9	0.18–0.28	5.1–6.1	—	0.10	0.50
(Max. solubility) (wt%)	5.8 at 548 K	0.14–0.86[43]	0.056 [44]	1.35[45] > 623 K Al$_6$Mn	17.4	<0.001	67.4	—	1.32 [46]	—

Table 3. Main precipitates families of the commercial aluminum alloys from the literature.

Alloy	Precipitate family 1	Precipitate family 1
2014	-	$CuAl_2$
2024	$CuMgAl_2$	$CuAl_2$
2124	$CuMgAl_2$	$CuAl_2$
5083	Al_3Mg_2 (grain boundaries)	Mg_2Si
6061	-	Mg_2Si
7010	$MgZn_2/Mg(Zn_2CuAl)$ (grain boundaries)	Al32(Mg, Zn)49
7050	$MgZn_2/Mg(Zn_2CuAl)$ (grain boundaries)	Al32(Mg, Zn)49
7075	$MgZn_2/Mg(Zn_2CuAl)$ (grain boundaries)	Al32(Mg, Zn)49

Table 4. Parameters in Equation (3) obtained from refs. [29, 52]. *Data have been linearly extrapolated beyond 20 MPa.

Parameter	Mg	Fe	Mn
Ω [m^3]		1.20e–29	
K		$1.38e^{-23}$	
α			
G [MPa]		30 659–15.614*T(K)	
M		3.06	
(A/B/C)		(-0.0011/0.043/-0.042)*	
D_{sol} [m^2 s^{-1}]	$6.2*10^{-6}*exp(-115000/RT)$	$7.1*10^{-1}*exp(-220000/RT)$	$1.5*10^{-2}*exp(-210000/RT)$
D_L [m2 s-1]		$7.1*10\_1*exp(-142000/RT)$	
Ln(r2/r1)		8	
Ln(c*/c$_0$*)		0.005	
C$_0$(%)		0.6	
β^2		$1.36e^{-60}$	

Figure 1. Normalized stress increment with respect pure aluminum data (Figure Ap.1, Supporting Information) versus normalized stress for commercial aluminum alloys (data taken from the literature).
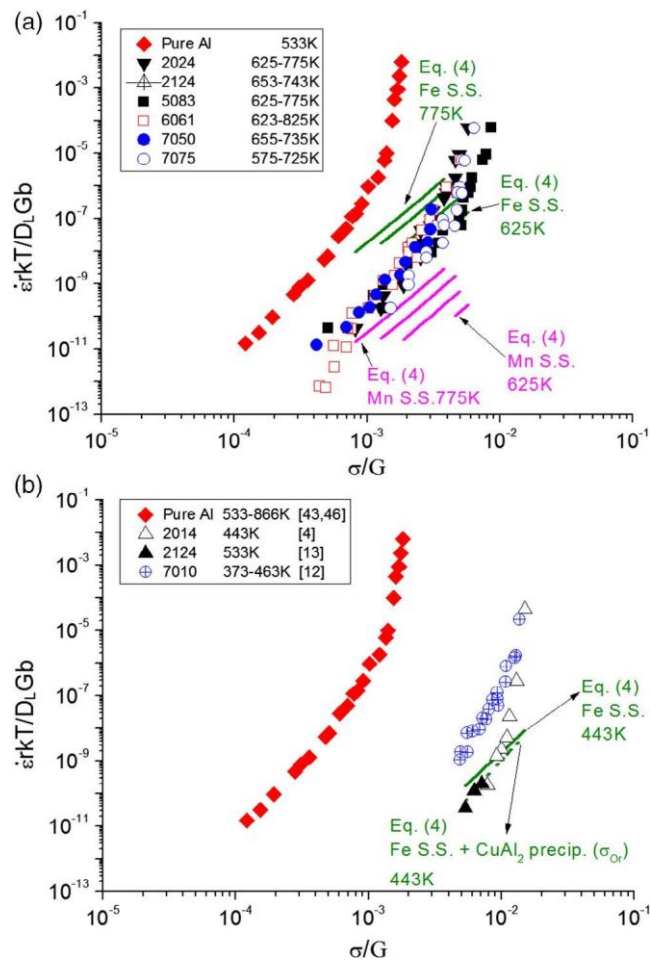
Figure 2. Normalized strain rate versus normalized stress for pure aluminum and aluminum alloys from the literature: a) above 550 K and b) below 550 K. Prediction of Equation (5) and (6) is shown. References are indicated into brackets.
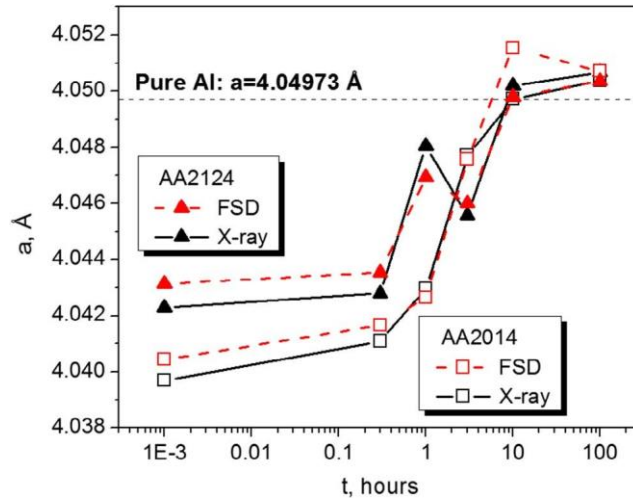
Figure 3. Aluminum lattice parameter evolution as a function of aging time at 523 K measured by neutron and XRD. Typical errors are 0.00005 Å.
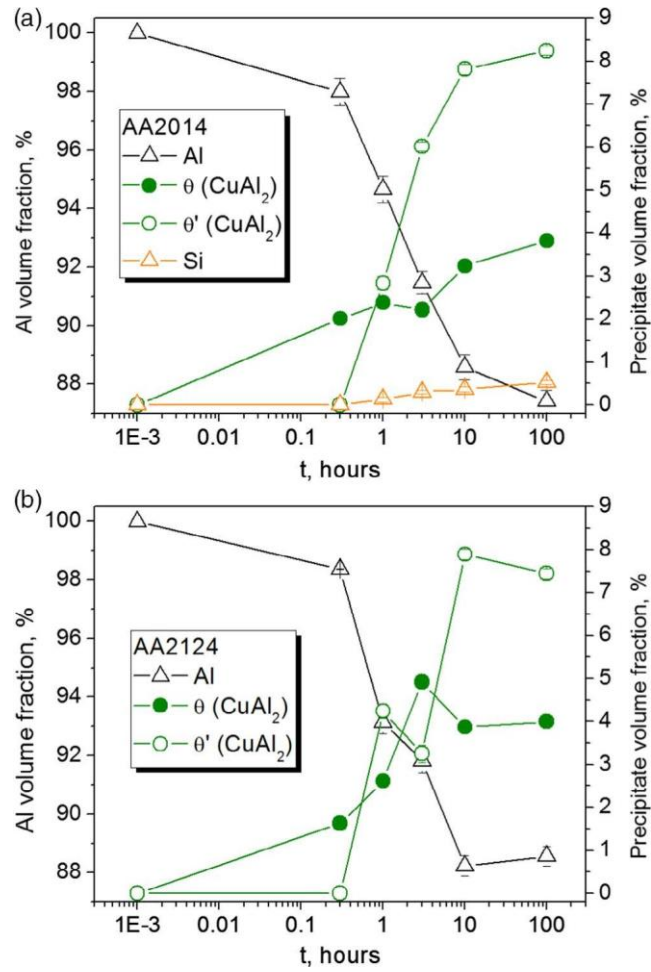
Figure 4. Aluminum and θ, $\theta´$ precipitates volume fraction evolution with aging time at 523 K: a) AA2014 alloy and b) AA2124 alloy.
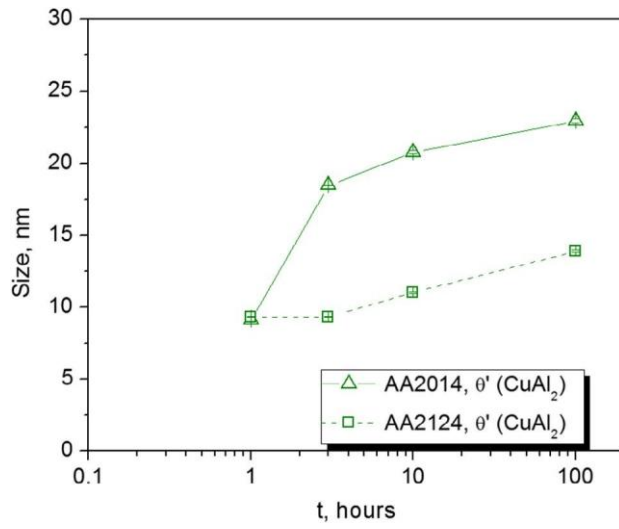
Figure 5. Semicoherent (small) precipitates θ' size evolution with aging treatment time at 523 K as extracted from Rietveld analysis of XRD data.
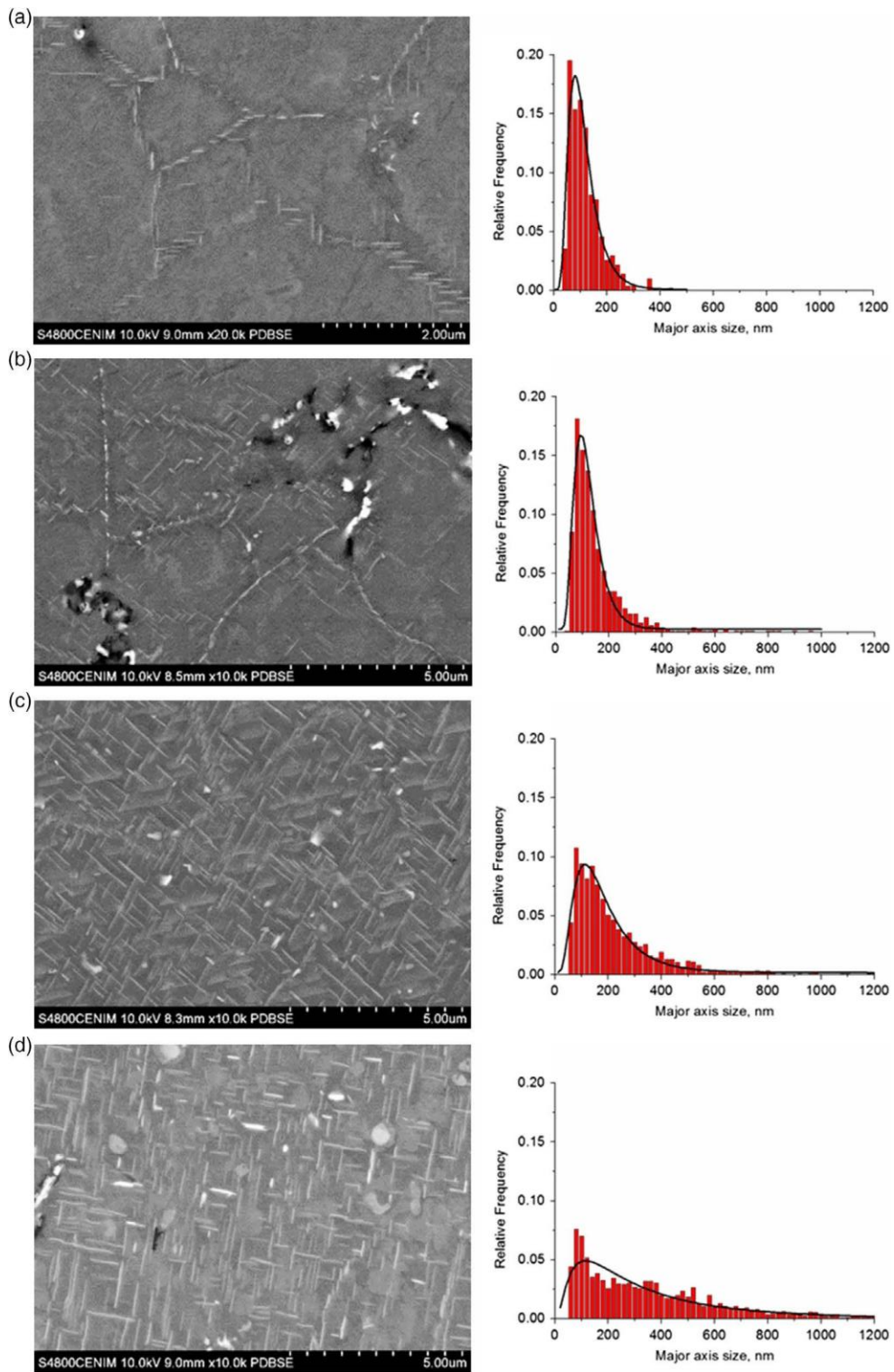
Figure 6. Typical precipitates appearance and size distribution for the AA2014 alloy at 523 K: a) 0.3 h, b) 1 h, c) 3 h, and d) 100 h. Mean size of precipitate's major axis is indicated into brackets.
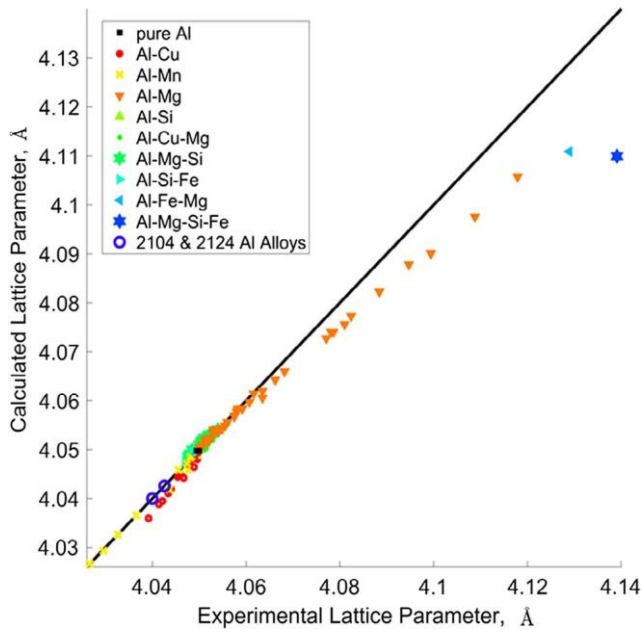
Figure 7. Unit cell parameters model predictions for binary, ternary, and quaternary systems, as well as AA2014 and AA2124 alloys. Comparison between the lattice parameter predicted by the model (Equation (2)) for binary, ternary, and quaternary systems as well as for the AA2014 and AA2124 alloys.
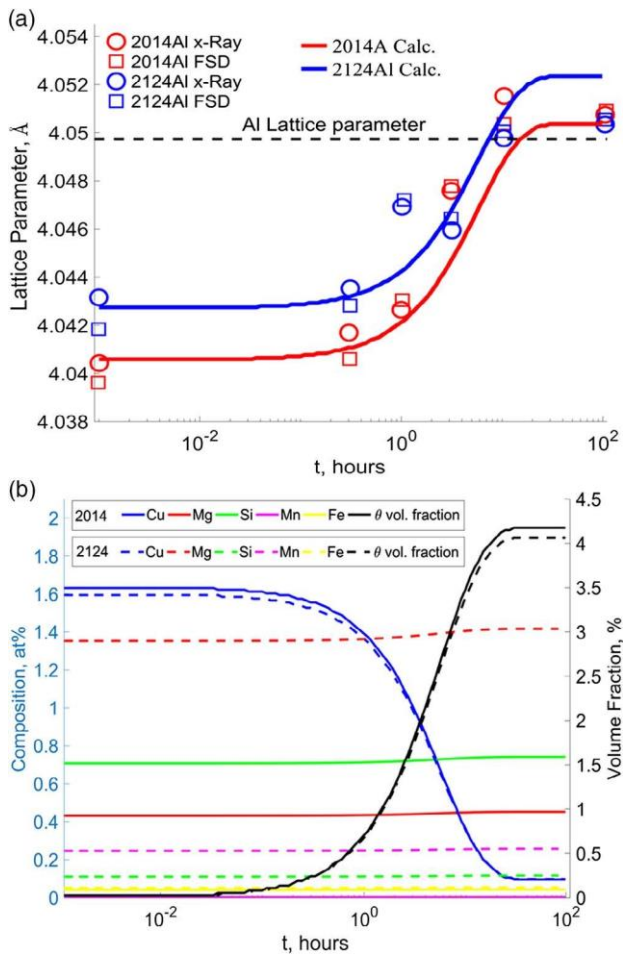
Figure 8. a) Composition evolution and θ precipitated volume fraction for both AA2014 and AA2124 alloys, and b) calculated and measured unit cell parameters at different times.
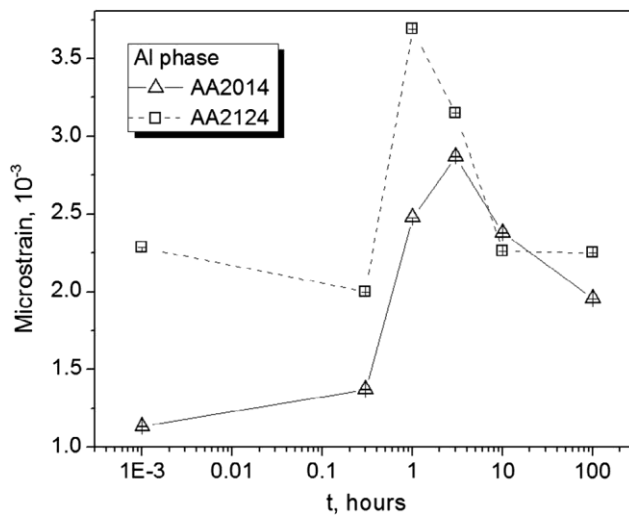

Figure 9. Microstrains for the Al phase estimated from peak broadening effect of XRD data.